Journal Information

ARTICLE

How to cite

Wolde et al. (2025). Biharmonic Trend Modeling with Sequential Gaussian Simulation for Geospatial Estimation of Soil Thickness. *East African Journal of Biophysical and Computational Sciences* Volume 6(2), 2025, 14-24

Open Access

Biharmonic Trend Modeling with Sequential Gaussian Simulation for Geospatial Estimation of Soil Thickness

Maregnesh Mechal Wolde[1,*]**, Zerihun Kinfe Birhanu**[1]**, Nils-Otto Kitterød**[2]

[1] Department of Mathematics, Hawassa University, Ethiopia.
[2] Soil and Water Science Section, Norwegian University of Life Sciences (NMBU), Ås, Norway

[*]Corresponding author: beharmech@gmail.com

Abstract

An integrated approach for soil thickness estimation is developed and evaluated. The method combines a biharmonic trend model with a stochastic Sequential Gaussian Simulation (SGS) component. Numerical experiments are first carried out in one dimentional synthetic data to provide a controlled enviroment for testing the methodology, investigating interpolation behavior, and determining parameter sensitivity. The approch is then extended to a two dimensional synthetic domain to see how well it captures spatial variability that is more representative of real-world applications. In both settings, the large-scale structure of the soil thickness field is approximated using a biharmonic equation, while the small-scale variability is represented by SGS applied to the residuals. This decomposition enables the method to preserve global smoothness imposed by the PDE model while simultaneously reproducing local heterogeneity through stochastic simulation. The results demonstrate that the hybrid method reduces prediction error relative to the PDE model or ordinary kriging alone, and that it provides a flexible approach for uncertainity quantification, making it suitable for realistic soil thickness mapping problems. .

Keywords: Soil thickness; Biharmonic PDE; Sequential Gaussian Simulation; Uncertainty .

1 Introduction

Soil thickness is an important variable in hydrological, ecological, and geo-engineering applications (Liu et al., 2013; Yan et al., 2021). Its estimation remains difficult because field observations are typically sparse, the terrain may vary rapidly, and measurements often contain noise. A recent study by Kitterød and Leblois (2021) introduced a Poisson's equation with a constant-curvature assumption. Although this formulation provides a useful representation of large-scale behaviour, the imposed curvature is restrictive and may not reflect the spatial variability observed in natural landscapes. Kitterød and Leblois (2021) assumed that large-scale sediment thickness and bedrock topography might be modeled as parabolic functions resembling the U-shaped forms common in glacial landscapes. Solution of the Poisson's equations are sensitive to boundary conditions, which makes it less realistic when boundary information is

uncertain. Stochastic methods, such as Sequential Gaussian Simulation (SGS), have been used to represent small-scale variability and quantify uncertainty. For example, Jamshidi et al. (2014) applied SGS to investigate soil erodibility at the catchment scale, demonstrating its ability to reproduce local heterogeneity and provide multiple realizations for uncertainty analysis. However, SGS depends on the choice of variogram model and does not incorporate physical constraints, which may reduce simulation results outside data clusters. These considerations motivate a combined approach. PDE-based methods provide physically consistent large-scale trends but are limited to account uncertainty, whereas SGS capture local variability but lack physical structure. A hybrid strategy can take advantage of both.

The objective of this study is to develop and assess a hybrid PDE-SGS approach for soil thickness estimation. The large-scale trend is modeled using a thin-plate biharmonic equation, a classical fourth-order elliptic PDE widely used for generating smooth surfaces and plate-bending approximations (Antonietti et al., 2018; Gazzola et al., 2010; Kumar, 2024; Timoshenko & Woinowsky-Krieger, 1959). In our formulation, the biharmonic operator is driven by data-informed load functions, allowing spatially varying curvature that adapts to the underlying terrain structure (Brenner & Scott, 2008). Small-scale variability is represented by applying SGS to the residual field, ensuring that stochastic fluctuations are consistent with the estimated spatial covariance model. The method is first tested in a controlled one-dimensional synthetic example where the exact solution is known, allowing a direct comparison between the numerical results and the exact solution. This environment enables a transparent presentation of the mathematical formulation and provides a direct means of verifying the finite element implementation of the biharmonic trend (Beirão da Veiga et al., 2013; Chinosi & Marini, 2006). Synthetic noise is introduced to mimic measurement uncertainty and to evaluate the reliability of the approach under realistic data conditions. The trend component is represented through a set of biharmonic basis functions whose coefficients are estimated from the data, while the SGS component generates multiple realizations that reproduce small-scale spatial structure. Predictive accuracy and uncertainty are assessed through resampling strategies, including leave-one-out cross-validation. The main contributions of this paper are:

1. construction of the soil-thickness trend using a biharmonic equation whose load functions are calculated directly from the observations,

2. incorporation of variability and uncertainty through Sequential Gaussian Simulation (SGS),

3. demonstration of the method's behaviour under sparse and noisy observations, and

4. development of a finite element implementation for the one-dimensional model.

Below, the general idea is outlined in Section 2, followed by an example of a one-dimensional solution in Section 3. The PDE-SGS procedure is presented in Section 4, while the finite element implementation is summarized in Section 5. Numerical results are provided in Section 6, and the discussion and conclusions are given in Sections 7 and 8.

2 Methodology

The method we propose combines PDE-based trend modelling with stochastic simulations. The proposed approach includes:

1. A PDE trend using the biharmonic operator to capture large-scale smooth trends in soil thickness.

2. A stochastic simulation component using Sequential Gaussian Simulation to model small-scale variability and uncertainty.

The hybrid solution is expressed as:

$$\mathbb{U}(x) = T(x) + R(x), \tag{1}$$

where $T(x)$ represents the ensemble realization of the trend obtained by solving a constrained biharmonic equation, and $R(x)$ represents the stochastic residual simulated using SGS.

3 Mathematics Formulation

We consider the following problem on a closed domain $\Omega \subset \mathbb{R}^n$:

$$\Delta^2 u = q \ \text{in} \ \Omega \tag{2a}$$

with boundary conditions:

$$u = 0 \quad \text{and} \quad \partial_n u = 0 \quad \text{on} \ \partial\Omega_{\mathrm{D}}, \tag{2b}$$

$$\Delta u = 0 \quad \text{and} \quad \partial_n(\Delta u) = 0 \quad \text{on} \ \partial\Omega_{\mathrm{N}}. \tag{2c}$$

The boundary $\partial\Omega = \partial\Omega_{\mathrm{D}} \cup \partial\Omega_{\mathrm{N}}$ is divided into a part $\partial\Omega_{\mathrm{D}}$ for Dirichlet boundary conditions and another $\partial\Omega_{\mathrm{N}}$ for Neumann boundary conditions. The right hand side function q will be referred to as the load function.

3.1 One-Dimensional Mathematical Formulation

We consider the one-dimensional case as a special instance of the general n-dimensional formulation in Sec. 3 with $n = 1$, i.e., the domain is $\Omega = [0, L]$. In this setting, the biharmonic equation (2a) - (2c) simplifies to

$$\frac{d^4u(x)}{dx^4} = q(x), \quad x \in \Omega, \tag{3a}$$

subject to homogeneous Dirichlet boundary conditions at the end points:

$$u(0) = 0, \qquad u(L) = 0, \tag{3b}$$

$$u'(0) = 0, \qquad u'(L) = 0, \tag{3c}$$

where the prime ($'$) denotes differentiation with respect to x. The load function $q(x)$ is expressed as:

$$q(x) = \sum_{i=1}^{n_d} p_i q_i(x), \qquad (3d)$$

where $q_i(x)$ are chosen load functions, p_i are unknown coefficients, and n_d is the number of basis functions (data points).

3.1.1 Variational (Weak) Formulation

Let V denote the function space that incorporates the essential (Dirichlet) boundary conditions of the problem:

$$V = \{\, v \in H^2(\Omega) \mid v(0) = v(L) = 0,\ v'(0) = v'(L) = 0 \,\}.$$

Functions in V therefore satisfy both the prescribed values and prescribed slopes at the boundary. To derive the weak formulation, we multiply (3a) by a test function $v \in V$ and integrate over the domain. Applying integration by parts twice and using the fact that both v and v' vanish at the boundaries yields the following weak problem:

Find $u \in V$ such that

$$\int_\Omega u''(x)\, v''(x)\, dx = \int_\Omega q(x)\, v(x)\, dx \quad \forall v \in V. \quad (4)$$

3.1.2 Discretization

To approximate the solution of the biharmonic (beam) problem, we employ the finite element method (FEM). The domain $[0, L]$ is partitioned into N uniform elements, with mesh points

$$0 = x_0 < x_1 < \cdots < x_N = L,$$

where $h = x_{i+1} - x_i$ denotes the uniform element length.

3.1.3 Basis functions: cubic Hermite polynomials

Since the Euler-Bernoulli beam equation involves both displacement and slope as nodal degrees of freedom, each element requires four degrees of freedom: $u(0)$, $u'(0)$, $u(h)$, and $u'(h)$. Accordingly, we adopt cubic Hermite polynomials as basis functions. This ensures C^1 continuity across elements, which are standard for fourth-order PDEs. On a reference element of length h, the beam profile is approximated as

$$u(x) = N_1^e u_1^e + N_2^e u_2^e + N_3^e u_3^e + N_4^e u_4^e,$$

where u_1^e, u_2^e are the displacement and slope at the left node, and u_3^e, u_4^e correspond to the right node. The cubic Hermite shape functions are given by

$$N_1^e = 1 - 3\frac{x^2}{h^2} + 2\frac{x^3}{h^3}, \qquad N_3^e = \frac{x^2}{h^2}\left(3 - 2\frac{x}{h}\right),$$

$$N_2^e = x\left(1 - 2\frac{x}{h} + \frac{x^2}{h^2}\right), \qquad N_4^e = \frac{x^2}{h}\left(\frac{x}{h} - 1\right).$$

The global finite element space $\mathbb{V}_h$ is formed by assembling these local Hermite basis functions over all elements. Imposing the clamped boundary conditions $u(0) = u(L) = 0$ and $u'(0) = u'(L) = 0$ sets the corresponding end functions to zero.

3.1.4 Discrete weak form

The approximate solution is expressed as

$$u_h(x) = \sum_{i=0}^{2N+1} c_i \phi_i(x),$$

with unknown coefficients c_i determined from the discrete weak form

$$a(u_h, \phi_j) = F(\phi_j), \qquad j = 0, 1, \ldots, 2N+1.$$

This leads to the linear system

$$\mathbf{K}_h \mathbf{U}_h = \mathbf{Q}_h,$$

where

$$(\mathbf{K}_h)_{ij} = \int_0^L \phi_i''(x)\, \phi_j''(x)\, dx, \qquad (\mathbf{Q}_h)_j = \int_0^L f(x)\, \phi_j(x)\, dx.$$

Here $\mathbf{K}_h$ and $\mathbf{Q}_h$ denote the stiffness matrix and load vector, respectively. Solving for $\mathbf{U}_h$ yields the finite element approximation $u_h(x)$.

3.2 Determination of Load Coefficients

To determine the unknown coefficients p_i, we enforce interpolation at the known data points (ξ_i, d_i):

$$u(\xi_i) = \sum_{j=1}^{n_d} p_j u_j(\xi_i) + u_{bc}(\xi_i) = d_i, \quad i = 1, \ldots, n_d. \quad (5)$$

This results in a linear system:

$$\underbrace{\begin{bmatrix} u_1(\xi_1) & u_2(\xi_1) & \cdots & u_{n_d}(\xi_1) \\ u_1(\xi_2) & u_2(\xi_2) & \cdots & u_{n_d}(\xi_2) \\ \vdots & \vdots & \ddots & \vdots \\ u_1(\xi_{n_d}) & u_2(\xi_{n_d}) & \cdots & u_{n_d}(\xi_{n_d}) \end{bmatrix}}_{A} \underbrace{\begin{bmatrix} p_1 \\ p_2 \\ \vdots \\ p_{n_d} \end{bmatrix}}_{P} = \underbrace{\begin{bmatrix} d_1 \\ d_2 \\ \vdots \\ d_{n_d} \end{bmatrix}}_{D} - \underbrace{\begin{bmatrix} u_{bc}(\xi_1) \\ u_{bc}(\xi_2) \\ \vdots \\ u_{bc}(\xi_{n_d}) \end{bmatrix}}_{},$$

$$AP = D. \qquad (6)$$

Upon solving (6), the load coefficients p_i are obtained. The PDE solution with n_d data points $\{(\xi_i, d_i)\}_{i=1}^{n_d}$ is then reconstructed as

$$u(x) = \sum_{i=1}^{n_d} p_i u_i(x) + u_{bc}(x), \qquad (7)$$

where u_i be the solutions of the biharmonic equations $\Delta^2 u_i = q_i$ with homogeneous Dirichlet boundary conditions for each of the load basis functions q_i, $i = 1, \ldots, n_q$. $u_{bc}(x)$ satisfies the boundary conditions alone.

4 Method Integration (PDE-SGS)

This section presents the combined approach that integrates the PDE-based trend reconstruction with Sequential Gaussian Simulation. The trend component is first estimated using the biharmonic PDE model, and its uncertainty is assessed through a leave-one-out cross-validation procedure. The resulting trend variance is then incorporated into the SGS algorithm to ensure that both spatial correlation and trend uncertainty are represented in the final realization. The overall approach yields spatial fields that honor the observed ata, the physical smoothness constraints enforced by the PDE, and the stochastic variability modeled through SGS.

4.1 Variance in the Trend Surface

To assess the uncertainty of the reconstructed trend, we employ a leave-one-out (LOO) analysis. At each iteration, one data point is removed, the trend surface is recomputed, and the excluded location is predicted. This procedure quantifies the sensitivity of the model to individual observations.

Formally, the ensemble of trend realizations is given by

$$T(x) = \{u^{(j)}(x)\}_{j=1}^{N_{\text{LOO}}}, \qquad (8)$$

where $u^{(j)}(x)$, $j = 1, \ldots, N_{\text{LOO}}$, denotes the surface obtained by excluding the jth point.

The mean trend surface is defined as

$$\bar{u}(x) = \frac{1}{N_{\text{LOO}}} \sum_{j=1}^{N_{\text{LOO}}} u^{(j)}(x), \qquad (9)$$

and the corresponding variance is

$$\sigma_T^2(x) = \frac{1}{N_{\text{LOO}} - 1} \sum_{j=1}^{N_{\text{LOO}}} \left(u^{(j)}(x) - \bar{u}(x)\right)^2. \qquad (10)$$

Thus, as a result, $T(x)$ in (1) can be replaced by the mean trend $\bar{u}(x)$, and the expression can be rewritten as

$$U(x) = \bar{u}(x) + R(x).$$

Residuals are then defined as

$$r_i = d_i - \bar{u}(\xi_i), \quad i = 1, \ldots, n_d. \qquad (11)$$

4.2 Sequential Gaussian Simulation (SGS)

Once the trend component has been obtained, the residuals (11) are treated as a stochastic field and modeled using Sequential Gaussian Simulation. SGS generates multiple equally probable realizations of a spatial variable that respect both the observed values and their spatial correlation structure (Deutsch & Journel, 1992; Gómez-Hernández & Srivastava, 2021). The variogram is the key input that characterizes this spatial dependence. In this work, an exponential variogram model is employed,

$$\gamma(h) = c_0 + c_1 \left(1 - \exp\left(\beta \left(\frac{h}{h_a}\right)^2\right)\right), \qquad (12)$$

where c_0 is the nugget, c_1 the partial sill, h_a the range, and $\beta = -\log(20)$, a commonly used shape parameter in geostatistical modeling, which determines the variance when $h = h_a$, and therefore is called the practical range. This model is chosen because it is flexible and widely used in practice. The estimated variogram parameters, reported in Section 6, are then used to simulate the residual field. SGS is carried out on a discretized grid of the domain. At each simulation step a grid node ξ_k is chosen at random from the unsimulated set. For the first unsampled location $x^* = \xi_{\kappa(1)}^*$, the conditioning data consist solely of the observed residuals,

$$\hat{\mathcal{C}}_0 = \{(\xi_i, r_i)\}_{i=1}^{n_d}.$$

Using ordinary kriging, the estimation at this location is expressed as

$$z_{OK}(x^*) = \sum_{i=1}^{n_d} \omega_i r_i, \qquad (13)$$

subject to the unbiasedness constraint

$$\sum_{i=1}^{n_d} \omega_i = 1,$$

where ω_i denotes the kriging weight assigned to the ith observation (Webster & Oliver, 2007). The weights are obtained by solving the linear system

$$\mathbf{Cov} \cdot \vec{x} = \mathbf{C}_{e,o},$$

where $\mathbf{Cov}$ is the covariance matrix of the observation points, $\mathbf{C}_{e,o}$ represents the covariance between the observations and the estimation point, and $\vec{x}$ contains the kriging weights and Lagrange multiplier. At x^*, the kriging mean $\mu(x^*) = z_{OK}(x^*)$ and the kriging variance $\sigma_R^2(x^*)$ are combined with the variance from the LOO-based trend surfaces, $\sigma_T^2(x^*)$ (10), to account for trend uncertainty. A simulated value is then drawn as

$$R(x^*) \sim \mathcal{N}\left(\mu(x^*), \sigma_R^2(x^*) + \sigma_T^2(x^*)\right).$$

This simulated value is appended to the conditioning set, and the procedure is repeated for the next unsimulated location along the random path. The process continues until all grid nodes are simulated, resulting in one complete realization of the residual field.

4.3 Final Reconstruction

The final realization is obtained by adding the PDE-based trend to the simulated residual field:

$$\mathbb{U}(x) = \bar{u}(x) + R(x). \tag{14}$$

Repeating this process with different random paths and draws (e.g., $K = 100$) yields an ensemble of realizations. These realizations reproduce both the large-scale PDE-based trend structure and the small-scale stochastic variability while honoring the observed data.

5 Implementation

The computational workflow is organized into three main stages: (i) verification of the finite element solver by comparison with a problem that admits an exact solution, (ii) estimation of the trend through a biharmonic formulation discretized by finite elements, and (iii) stochastic modeling of the residual component using sequential Gaussian simulation (SGS).

5.1 Computing the Biharmonic Equation Analytically

Before applying the method to synthetic data, we verify the finite element implementation against a biharmonic problem that admits a closed-form analytical solution. Such verification is standard practice in numerical analysis and finite element development (Braess, 2007; Brenner & Scott, 2008). The one-dimensional biharmonic equation corresponds to the classical clamped Euler-Bernoulli beam equation (Szabó & Babuška, 2021; Timoshenko & Goodier, 1951):

$$u^{(4)}(x) = 1, \qquad x \in [0, L], \tag{15a}$$

with clamped boundary conditions

$$u(0) = u(L) = 0, \qquad u'(0) = u'(L) = 0. \tag{15b}$$

Integrating (15a) four times yields

$$u(x) = \frac{1}{24}x^4 + Ax^3 + Bx^2 + Cx + D.$$

Imposing the clamped conditions (15b) at $x = 0$ gives $C = D = 0$. The remaining conditions $u(L) = 0$ and $u'(L) = 0$ lead to

$$\frac{1}{24}L^4 + AL^3 + BL^2 = 0,$$
$$\frac{1}{6}L^3 + 3AL^2 + 2BL = 0.$$

Solving this system yields

$$A = -\frac{L}{12}, \qquad B = \frac{L^2}{24}.$$

Thus, the exact analytical solution is

$$u_{\text{exact}}(x) = \frac{1}{24}x^4 - \frac{L}{12}x^3 + \frac{L^2}{24}x^2, \tag{16}$$

which is the unique polynomial satisfying the biharmonic operator and clamped boundary conditions (Timoshenko & Goodier, 1951). To evaluate the accuracy of the finite element approximation u_h, we compute the discrete maximum and L^2 norms of the error at the computational nodes x_j:

$$\|e\|_\infty = \max_j \left| u_{\text{exact}}(x_j) - u_h(x_j) \right|, \tag{17a}$$

$$\|e\|_2 \approx \left(\sum_j \left| u_{\text{exact}}(x_j) - u_h(x_j) \right|^2 \Delta x_j \right)^{1/2}. \tag{17b}$$

These metrics allow us to compare numerical results with the analytical solution and to verify the expected convergence behavior of the biharmonic finite element discretization (Braess, 2007; Brenner & Scott, 2008).

5.2 One-Dimensional Biharmonic Trend Estimation

We model the trend as the solution of a biharmonic boundary value problem on the interval $\Omega = [0, L]$, with clamped boundary conditions (3b) and (3c). The weak form (4) is discretized using cubic Hermite shape functions on a uniform mesh of N elements. The resulting stiffness matrix denoted by $\mathbf{K}_h$: $\mathbf{K}_h \in \mathbb{R}^{2(N+1) \times 2(N+1)}$ corresponds to the finite element discretization of the biharmonic operator (3a). External forcing is represented by Gaussian load functions centered at the data points:

$$q_i(x) = \frac{1}{\sigma\sqrt{2\pi}} \exp\left(-\frac{1}{2}\left(\frac{x - \xi_i}{\sigma}\right)^2 \right), \quad i = 1, \ldots, n_d, \tag{18}$$

with a set of synthetic data points $\{(\xi_i, d_i)\}_{i=1}^{n_d}$. The trend is constructed as a linear combination of solution of (3a), each $u_j(x)$ corresponding to a Gaussian load centered at ξ_i (18):

$$u(x) = \sum_{j=1}^{n_d} p_j\, u_j(x),$$

where the coefficients p_j are determined by enforcing interpolation at the observation points.

6   Results

6.1   Comparison with the Exact Solution

As an initial verification, we consider the biharmonic boundary-value problem (15) on the domain $x \in [0, 10]$, where the exact solution (16) is expressed as:

$$u_{\text{exact}}(x) = \frac{1}{24}x^4 - \frac{5}{6}x^3 + \frac{25}{6}x^2.$$

We solved the discrete biharmonic problem using the cubic-Hermite finite-element formulation described in Sec. 3.1.3, and the comparison with the exact solution is shown in Figure 1. This test is especially useful because the forcing term is constant, and the exact solution is a smooth polynomial. As a result, it allows for a quick but careful evaluation of our finite element solver's accuracy and boundary condition implementation. Table 4 and Figure 1 summarize the error norms and condition numbers for uniformly refined meshes. The infinity norm and L^2 error in (17) decrease rapidly for the finer mesh, indicating the accuracy of the finite element discretization. The condition number increases proportionally to h^{-4}, where h represents the mesh size. This is consistent with the theoretical behavior of stiffness matrices associated with fourth-order operators (Ciarlet & Raviart, 1972).

6.2   Application of the PDE to Synthetic Data

The methodology was implemented on a synthetic 1D dataset after comparing the numerical and exact solutions. The computational domain was defined on $[0, 10]$ with $n_d = 14$ irregularly spaced observation points: $\{(\xi_i, d_i)\}_{i=1}^{n_d}$. The soil thickness data are

$d = \{1.5, 1.7, 2.0, 2.05, 2.5, 2.8, 3.0, 3.3, 3.8, 0.2, 1.0, 0.6, 4.5, 4.0\}$, at the corresponding locations

$\xi = \{6.0, 13.0, 7.0, 9.0, 11.0, 13.0, 8.0, 6.0, 27.0, 10.0, 9.0, 10., 15.0, 18.0\}$.

The biharmonic formulation (3a) was updated with a Gaussian load function (18) and cubic Hermite finite element discretization was used to create the basis functions. The biharmonic trend estimator is a linear combination of basis functions, with coefficients obtained by solving system (6) using observed data (Figure 2, **A**). Near $x = 4$, two closely spaced data points (Figure 2, **A**, marked by ◆) caused small oscillations in the solution. To reduce artifacts and avoid negative soil thickness estimation, the two points were replaced with their average. The adjusted biharmonic trend is shown in (Figure 2, **B**), where the averaged point is indicated by ■, demonstrating the method's ability to capture smooth large-scale variations while suppressing spurious fluctuations. To account for uncertainty in the trend, 14 realizations (8) were generated using the sensitivity analysis described in Sec. 4.1. The variance was computed using

Equation (10), and the mean trend defined in Equation (9) was used as a reliable estimate of the underlying trend(Figure 2 (**C**)).

6.3   Choice of Load Functions

In our study, we implemented two types of load functions to drive the biharmonic equation: the Dirac delta and the Gaussian function. The Dirac delta function, $\delta(x - \xi_i)$, represents an idealized point load concentrated exactly at a given observation location ξ_i, $i = 1, \cdots, n_d$. Numerically, it can be implemented either as a discrete spike at the nearest grid point. Using the Dirac delta load minimizes oscillations when data points are closely spaced, and thus improves the numerical stability of the biharmonic solution. However, the physical meaning of the load is better captured by the Gaussian function, which distributes the influence of each observation over a small region controlled by a spread parameter σ. The Gaussian load gradually decreases away from the center, representing a more realistic distributed effect of each data point on the sediment soil thickness surface (Figure 2, A), because soil thickness is most likely a smooth process in space. Therefore, while the Dirac delta is useful for testing numerical performance, the Gaussian function provides a physically meaningful approximation of the influence of each observation on the surface construction of two dimentional case.

6.4   Application Sequential Gaussian Simulation

The Sequential Gaussian Simulation procedure from Sec. 4.2 was applied under two data settings to capture both large-scale trends and small-scale variability (Figure 3).

1. **SGS on the raw data (Ordinary Kriging setting).** In this case, the trend component is set to zero, and SGS is applied directly to the observed (synthetic) soil-thickness values to obtain an ordinary kriging-type estimate. (Figures 4, **A** and **C**) show a single SGS realization and the mean of 100 realizations, respectively.

2. **SGS on the residual field.** To incorporate uncertainty and capture small-scale variability, SGS was applied to the residuals obtained after removing the biharmonic trend. Multiple realizations were generated by sampling from conditional Gaussian distributions at unsampled locations. (Figure 4 , **B**) compares a single realization with the mean of hundreds of leave-one-out (LOO) realizations, while (Figure 4 , **D**) compares a single realization with the average of 100 realizations based on all residual data. The final hybrid field was reconstructed by adding the SGS residuals to the biharmonic trend (14), resulting in a surface that combines smooth large-scale structure with localized stochastic fluctuations.
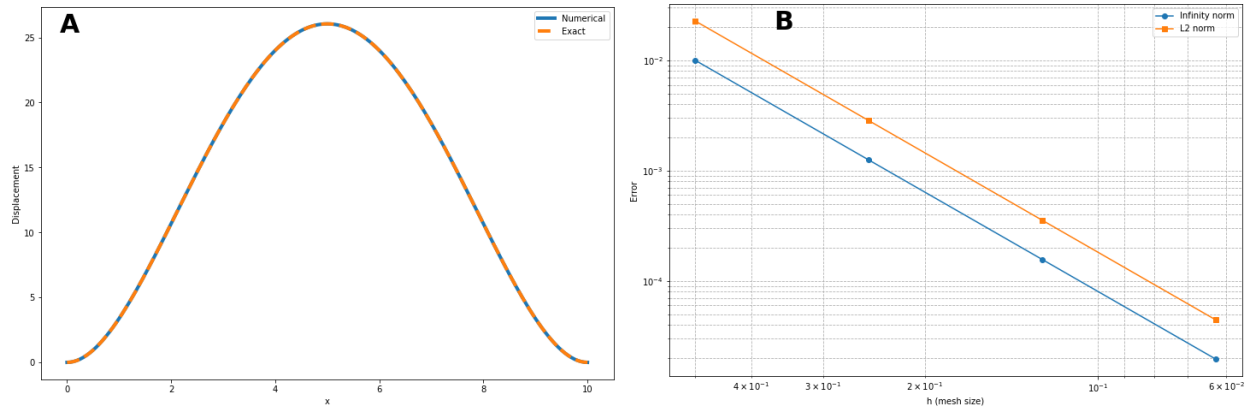
Figure 1: **A**: comparison of the numerical (15b) and exact (16) solutions; **B**: log–log plot of the errors in the infinity norm ($\|e\|_\infty$) and in the L_2 norm (17).
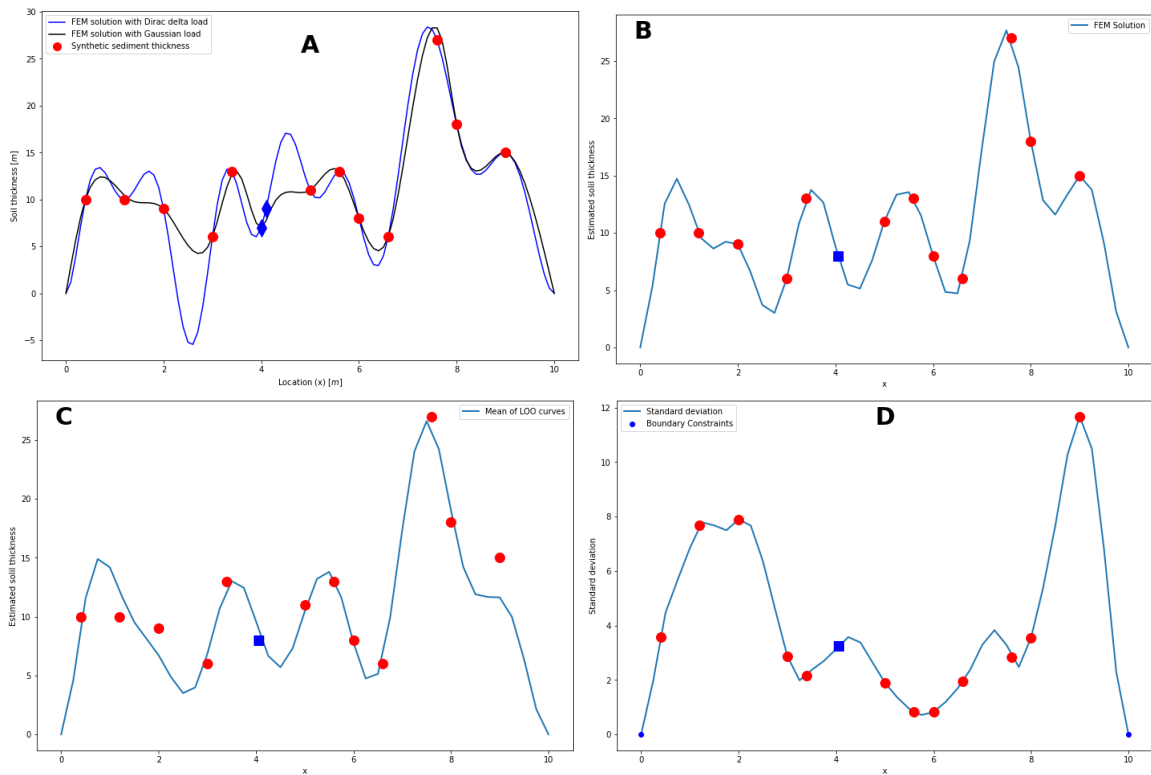

Figure 2: **A**: Interpolation at data points (6) and (7); **B**: local averaging; **C**: average of leave-one-out estimation(9); **D**: Standard deviation of the LOO curves (10).
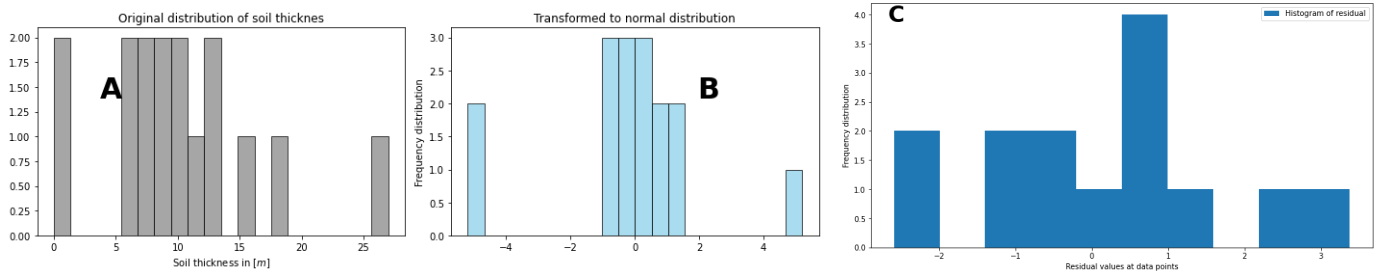

Figure 3: **A**: Histogram of synthetic soil thickness (11); **B**:Histogram of transformed soil thickness; **C**: Histogram of residual (14).

6.5 Comparison of Modeling Approaches

Based on Table 1, the variogram parameters estimated for the Ordinary Kriging (OK) and Hybrid (Trend + SGS)

models differ significantly, reflecting that each model captures distinct underlying spatial structures. The smaller sill in the Hybrid model indicates that the residual variance is lower,
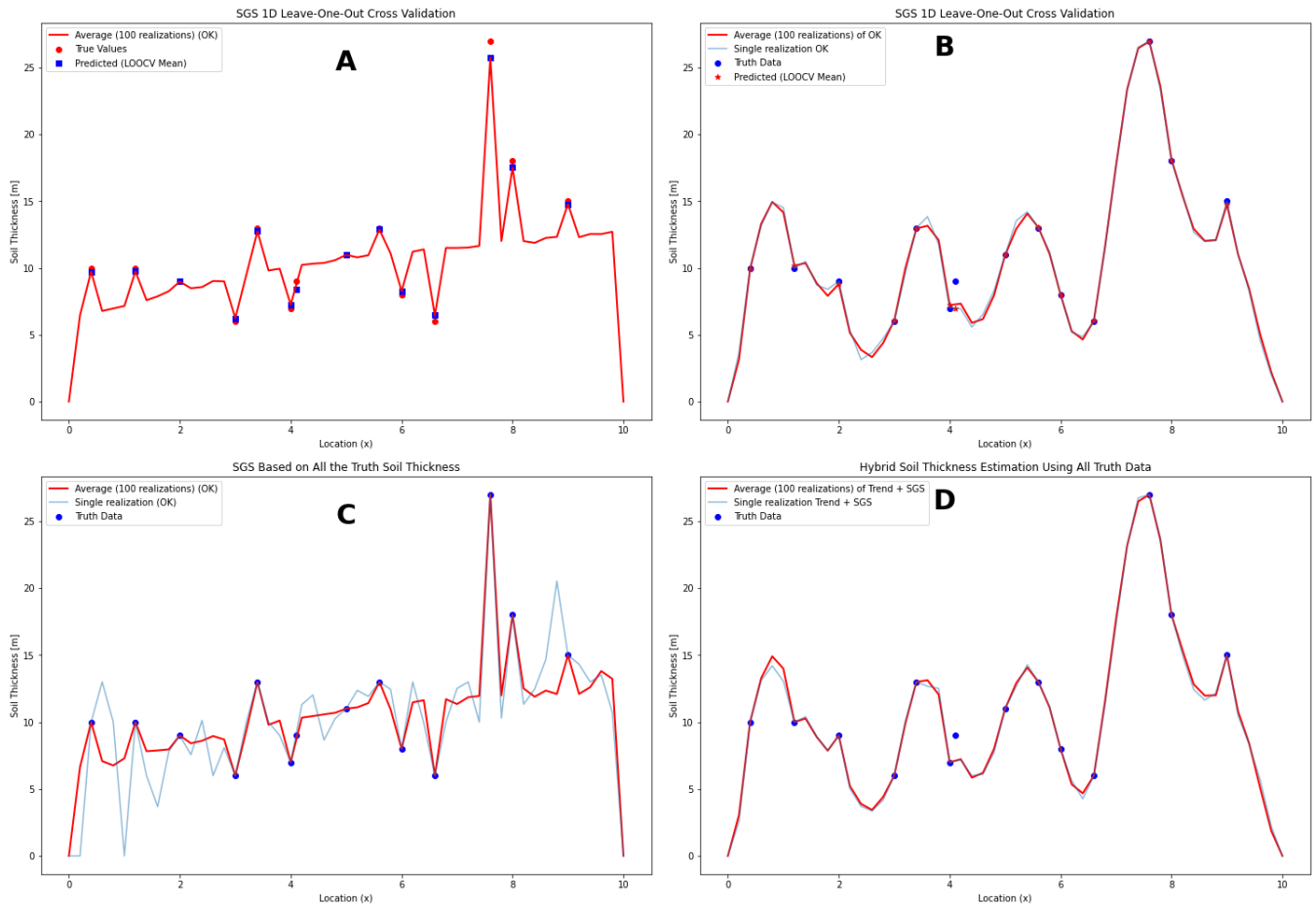
Figure 4: **A**: SGS (Ordinary Kriging estimation) applied directly to the raw data using LOO cross-validation. **B**: SGS applied to the residual field using LOO, combined with the biharmonic trend (14). **C**: SGS(OK) of all synthetic soil-thickness data. **D**: SGS of the residual computed from all synthetic soil-thickness, combined with the biharmonic trend.) (14).

confirming that the stochastic component primarily captures local fluctuations around the physically based trend. The slightly larger range in the Hybrid also suggests improved spatial continuity of the residuals, implying that spatial correlation persists over longer distances. These variogram characteristics demonstrate that the Hybrid approach achieves a better balance between global smoothness and local variability compared to the OK model alone.

(Table 2 and 3) summarizes the performance of the three modeling approaches: the PDE-based trend model, Ordinary Kriging (OK), and the hybrid approach (Trend + SGS), in terms of Mean Absolute Error (MAE), relative Mean Absolute Error (RMAE), and the coefficient of determination (R^2). The error criterias (Table 3) indicate a substantial improvement in model performance when moving from the PDE-based trend model to the OK and hybrid methods.

Ordinary kriging provides smooth estimates by definition, but it assumes second-order stationarity. By modeling the trend separately, we instead assume first-order stationarity of the residuals, allowing for better representation of local variations while maintaining a reasonable large-scale structure (Figure 4, **A**, **C**). The error criteria for OK are MAE = 0.404, RMAE = 0.035, and R^2 = 0.992, indicating good local accuracy but limited global structural representation. The PDE-based trend model

produces a smooth, curvature-driven surface that captures the majority of the large-scale spatial variability while maintaining physical consistency across the domain (Figure 2, **C**). The error metrics are MAE = 0.966, RMAE = 0.083, and R^2 = 0.970 . This demonstrates that the trend model provides a globally coherent and physically meaningful estimation but underestimates local variations near measurement points due to the lack of a stochastic component.

The Hybrid approach (Trend + SGS) achieves the best overall performance by combining the PDE-based trend with a stochastic residual component. This integration captures soil thickness variability at both large and fine scales. The Hybrid model has the lowest errors, MAE = 0.326, RMAE = 0.028, and the highest coefficient of determination, R^2 = 0.993. It preserves the physically consistent trend of the PDE model while incorporating the local variability represented by the stochastic Gaussian simulation (SGS) (Figure 4, **B, D**).

Table 1: Estimated variogram parameters for Ordinary Kriging (OK) (Raw data) and Hybrid (Trend + SGS) models (residual).

Model	Nugget	Sill	Range
Ordinary Kriging (OK)	4.69	13.39	24.07
Hybrid (Trend + SGS)	1.96	3.76	27.50

Table 2: Sorted data by ascending Location

Location	Synthetic Soil Thickness	OK	Trend	Hybrid
0.4	10	9.73	8.95	9.97
1.2	10	9.75	12.22	10.33
2.0	9	8.98	6.73	9.08
3.0	6	6.25	6.83	6.09
3.4	13	12.74	12.38	12.96
4.0	7	7.25	9.59	7.21
4.1	9	8.43	8.29	7.23
5.0	11	10.98	10.45	11.02
5.6	13	12.88	13.24	13.06
6.0	8	8.27	7.76	8.04
6.6	6	6.46	6.56	6.11
7.6	27	25.74	26.18	26.98
8.0	18	17.52	19.02	18.15
9.0	15	14.79	11.62	15.00

Table 3: Validation criterias for the three methods

Method	MAE	RMAE	R^2
OK	0.404	0.035	0.992
Trend	0.966	0.083	0.970
Hybrid	0.326	0.028	0.993

Formulas:

$$\text{MAE} = \frac{1}{n}\sum_{i=1}^{n}|y_i - \hat{y}_i|, \quad \text{RMAE} = \frac{\text{MAE}}{\bar{y}}, \quad R^2 = 1 - \frac{\sum_{i=1}^{n}(y_i - \hat{y}_i)^2}{\sum_{i=1}^{n}(y_i - \bar{y})^2}$$

where y_i is the synthetic soil thickness at location i, $\hat{y}_i$ is the predicted value at location i, n is the total number of data points, $\bar{y}$ is the mean of synthetic soil thickness.

6.6 Two-Dimensional (Gaussian Spread)

We extend the proposed methodology to a two-dimensional setting governed by the biharmonic plate equation (2a) -(2c). The numerical experiments are designed to reconstruct soil thickness trend and to estimate the unknown coefficients p_i associated with the Gaussian load functions centered at the synthetic observation locations $\tilde{\xi}_i$ (18). The parameter σ controls the spatial spread of each Gaussian load. A small value such as $\sigma = 0.1$ yields a more localized load distribution and results in reduced oscillations in the reconstructed surface compared with a wider kernel (e.g., $\sigma = 0.5$). The larger σ spreads the load over a broader region, causing interactions between nearby observation points and introducing additional oscillatory artifacts in the solution (Figure 5 and 6).

In this experiment, we use the soil thickness data

$\tilde{d}$ = (1.6, 1.2, 0.6, 1.6, 2.0, 1.0, 2.0, 1.8, 0.8, 2.4, 0.9, 0.7, 1.0, 0.5, 0.6), at the locations

$\tilde{\xi}$ = {(3.0, 5.0), (6.0, 5.5), (8.0, 7.0), (5.0, 7.0), (7.0, 7.0), (3.0, 7.5), (3.1, 3.0), (4.0, 6.0), (5.0, 6.0), (5.1, 6.1), (6.0, 4.0), (8.0, 2.0), (5.0, 4.0), (7.0, 5.0), (9.0, 1.5)}.

Table 4: Error norms and condition numbers for the problem in Figure 1, solved with FEM on the interval $[0, 10]$ using cubic Hermite elements.

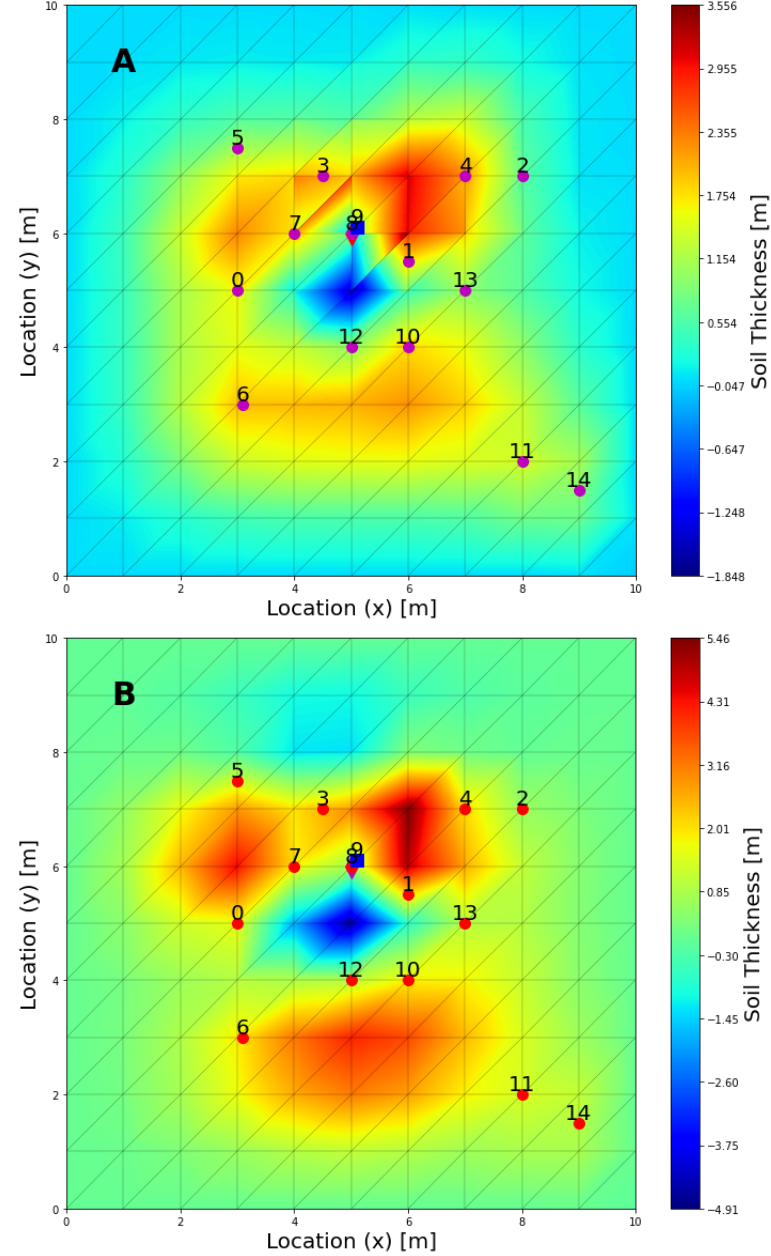| N	h	$\|e\|_\infty$	$\|e\|_2$	$cond(\mathbf{K}_h)$
20	5.000×10^{-1}	1.000×10^{-2}	2.273×10^{-2}	1.71×10^4
40	2.500×10^{-1}	1.250×10^{-3}	2.841×10^{-3}	2.75×10^5
80	1.250×10^{-1}	1.566×10^{-4}	3.552×10^{-4}	4.41×10^6
160	6.250×10^{-2}	1.958×10^{-5}	4.440×10^{-5}	7.06×10^7

Figure 5: (**A**) Two-dimensional interpolation results with $\sigma = 0.1$. (**B**) Two-dimensional interpolation results with $\sigma = 0.5$. The points ■ and ◆ highlight the two data points responsible for the observed oscillation.
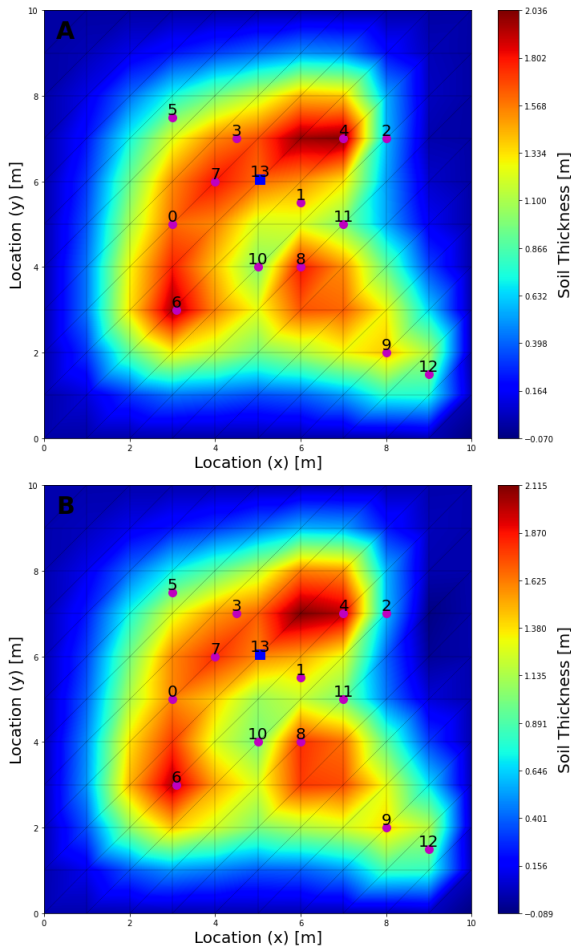
Figure 6: Results after replacing the two data points (shown as ■ and ♦ in Figure 5) with their averaged value. (**A**) uses $\sigma = 0.1$, and (**B**) uses $\sigma = 0.5$.

are sparse or where the measured values exhibit sharp deviations from the surrounding trend. Interpolation-related limitations. The study also revealed limitations when interpolation is used directly on the data without regularization. In particular, when observations lie very close to each other as illustrated by the points marked with ■ and ♦ the interpolant may develop oscillations in the reconstructed surface. This behavior is visible in both one-dimensional and the two-dimensional examples (Figures 4, **A** , Figures 5, **A** and **B**) and is a well-known artifact of high-order interpolation on irregularly spaced data. Local averaging of the problematic points reduces these oscillations (Figures 4, **B**, Figures 6, **A** and **B**) and leads to a more stable surface while preserving the general structure of the dataset. To construct the two-dimensional discrete form of (2), we used the DUNE approach (Bastian et al., 2021). The `dune-vem` module enables the use of $\mathcal{C}^1$-conforming virtual element spaces, which provide a smooth representation suitable for the biharmonic equation. This formulation reduces the number of degrees of freedom relative to classical finite elements without sacrificing accuracy (Beirão da Veiga et al., 2013; Dedner & Hodson, 2024). In addition, the choice of the kernel width σ in (18) affects the smoothness and flexibility of the basis functions: larger values of σ allow sharper local variations, while smaller values produce smoother surfaces. The numerical experiments in 2D (Figures 5, **A** and **B**) illustrate this influence.

Overall, the combination of a biharmonic trend and a stochastic residual model provides a balance between physical smoothness and local variability. The trend offers global coherence, while SGS supplies the fine-scale fluctuations needed to represent the observed soil thickness. The 1D tests verify the correctness of the approach and clarify the role of each component before applying the method to more complex two-dimensional domains.

7 Discussion

The one-dimensional experiments were carried out to examine the behavior of the proposed approach in a controlled setting where the exact solution is known (Figure 1). This allows a transparent assessment of how the biharmonic trend model and the stochastic residual component contribute to the final estimate. The results show that the biharmonic trend captures the large-scale structure of the soil profile and produces a smooth background surface. This smoothness arises naturally from the biharmonic operator and prevents the type of overfitting that may occur when interpolation is applied directly to sparse or unevenly spaced data (Figure 2). The trend is therefore well suited for representing the slowly varying component of the soil thickness field. The stochastic component introduced through SGS adds the local variability that the PDE-based trend cannot reproduce. Because SGS simulates conditional realizations using the estimated variogram structure, it preserves the spatial correlation observed in the data while introducing realistic small-scale fluctuations. The ensemble of SGS realizations provides a measure of uncertainty, and the variance field highlights regions where predictions become less reliable. As expected, these areas coincide with locations where observations

8 Conclusion

The hybrid PDE-SGS method demonstrates advantages over the individual components, providing improved predictive accuracy and a more realistic representation of soil thickness variability. While the present study focuses on one-dimensional and regular two-dimensional domains to verify the mathematical formulation and numerical implementation, the framework naturally extends to irregular two-dimensional settings. In such cases, the treatment of boundary conditions becomes more practical. To clarify this point, we now refer the reader to our extended work (Bekele et al., 2025), where we have already implemented a mixed, data-driven boundary (domain) strategy: observed data are used to prescribe boundary values along measured boundary segments, while Neumann conditions are applied on segments lacking observations. As demonstrated in (Bekele et al., 2025), this approach enhances the physical realism of the reconstructed soil-thickness surfaces.

Acknowledgments

Funding

Conflict of interest

The authors declare that they have no conflict of interest.

References

Antonietti, P. F., Manzini, G., & Verani, M. (2018). The fully nonconforming virtual element method for biharmonic problems. *Mathematical Models and Methods in Applied Sciences*, *28*(2), 387–407. https://doi.org/10.1142/S0218202518500100

Bastian, P., Blatt, M., Dedner, A., Dreier, N. A., Engwer, C., Fritze, R., Grser, C., Grninger, C., Kempf, D., Klfkorn, R., Ohlberger, M., & Sander, O. (2021). The dune framework: Basic concepts and recent developments. *Computers & Mathematics with Applications*, *81*, 75–112.

Beirão da Veiga, L., Brezzi, F., Cangiani, A., Manzini, G., Marini, L. D., & Russo, A. (2013). Basic principles of virtual element methods. *Mathematical Models and Methods in Applied Sciences*, *23*(1), 199–214.

Bekele, S. S., Wolde, M. M., Führer, C., Kitterød, N.-O., & Kværnø, A. (2025). Modeling a smooth surface by a constrained biharmonic equation with application in soil science. https://arxiv.org/abs/2510.23195

Braess, D. (2007). *Finite elements: Theory, fast solvers, and applications in solid mechanics* (3rd ed.). Cambridge University Press.

Brenner, S. C., & Scott, L. R. (2008). *The mathematical theory of finite element methods* (3rd ed., Vol. 15). Springer.

Chinosi, C., & Marini, L. D. (2006). A virtual element method for the biharmonic problem. *Computers & Structures*, *84*(13–14), 914–923.

Ciarlet, P. G., & Raviart, P. A. (1972). Finite element approximation of the biharmonic problem. *Numerische Mathematik*, *18*(4), 335–348.

Dedner, A., & Hodson, A. (2024). A framework for implementing general virtual element spaces. *SIAM Journal on Scientific Computing*, *46*(3), B229–B253. https://doi.org/10.1137/23M1573653

Deutsch, C. V., & Journel, A. G. (1992). Geostatistical software library and users guide. *New York*.

Gazzola, F., Grunau, H.-C., & Sweers, G. (2010). *Polyharmonic boundary value problems* (Vol. 1991). Springer.

Gómez-Hernández, J. J., & Srivastava, R. M. (2021). One step at a time: The origins of sequential simulation and beyond. *Mathematical Geosciences*, *53*(2), 193–209.

Jamshidi, R., Dragovich, D., & Webb, A. A. (2014). Catchment scale geostatistical simulation and uncertainty of soil erodibility using sequential gaussian simulation. *Environmental Earth Sciences*, *71*(12), 4965–4976.

Kitterød, N.-O., & Leblois, É. (2021). Estimation of sediment thickness by solving poisson's equation with bedrock outcrops as boundary conditions. *Hydrology Research*, *52*(3), 597–619.

Kumar, R. (2024). Numerical solutions for biharmonic interface problems via weak galerkin finite element methods. *Applied Mathematics and Computation*, *467*, 128496. https://doi.org/10.1016/j.amc.2023.128496

Liu, Q., West, A. J., & Dietrich, W. E. (2013). A simple geomorphic-based analytical model for predicting the spatial distribution of soil thickness in headwater hillslopes and catchments. *Water Resources Research*, *49*(10), 7029–7046. https://doi.org/10.1002/2013WR013834

Szabó, B. A., & Babuška, I. (2021). *Applied finite element analysis* (2nd ed.). John Wiley & Sons.

Timoshenko, S. P., & Goodier, J. N. (1951). *Theory of elasticity* (2nd ed.). McGraw–Hill.

Timoshenko, S. P., & Woinowsky-Krieger, S. (1959). *Theory of plates and shells* (2nd ed.). McGraw-Hill.

Webster, R., & Oliver, M. A. (2007). *Geostatistics for environmental scientists* (2nd ed.). John Wiley & Sons.

Yan, Q., Wainwright, H., Dafflon, B., Uhlemann, S., Falco, N., Kwang, J., & Hubbard, S. (2021). A hybrid data–model approach to map soil thickness in mountain hillslopes. *Earth Surface Dynamics*, *9*, 1347–1367. https://doi.org/10.5194/esurf-9-1347-2021